Journal of the Indian Institute of Science
A Multidisciplinary Reviews Journal
ISSN: 0970-4140 Coden-JIISAD

REVIEWS

A Review of Atmospheric Wind Speed Measurement Techniques with Shack Hartmann Wavefront Imaging Sensor in Adaptive Optics

*M.B. Roopashree[1], Akondi Vyas[2] and B. Raghavendra Prasad[1]**

Abstract | Atmospheric wind speed is an turbulence parameter that determines turbulence coherence scales and plays a key role in the optimal performance of the adaptive optical system. Real time monitoring of atmospheric wind speed can allow better wavefront sensing. The use of the Shack Hartmann wavefront sensor (SHWS) for the measurement of atmospheric wind speed is well known. This article illustrates with some of the techniques that extract wind speed from the slope measurements of the SHWS. Laboratory experiments demonstrate the usefulness of the SHWS in accurately determining wind speed in real time.

1 Introduction

A meticulous characterization of atmospheric turbulence is a prerequisite for designing adaptive optics systems for large ground based astronomical telescopes. Atmospheric turbulence is defined through the refractive index structure constant profile, $C_n^2(h)$ and wind profile, $v(h)$ as a function of altitude, h. The performance of an adaptive optics system is dictated by a large number of atmospheric factors derived from $C_n^2(h)$ and $v(h)$ including Fried's parameter (r_0), isoplanatic angle (θ_0), coherence time (τ_0) and instrument constraints like wavefront sensor induced error, wavefront corrector residual error and finite bandwidth.[1] The complex correlation between these parameters makes the design of an adaptive optics system a challenging optimization problem.[2,3] There exists significant temporal variability of Fried's parameter and wind velocity which is also site dependent.[4–6] Hence it is important to continuously monitor the turbulence parameters to maintain the consistency of performance in an adaptive optics system. This can be done by controlling a few adaptive optical system parameters. In this article, the methods of detecting these fluctuations in wind velocity which help in enhancing the performance of adaptive optics systems are elaborated.

It was shown that atmospheric wind velocity profile has a complex relationship with other adaptive optics parameters.[7] Wind velocity controls intensity variations and temporal frequency of wavefront fluctuations. Observations of stellar scintillations by Hufnagel[8] showed good correlation of intensity with square of the average of vertically integrated wind velocity. The profile $C_n^2(h)$ following Hufnagel-Valley turbulence model (including surface turbulence correction by Valley[9] is defined as,

$$C_n^2(h) = s_1 h^{10}\left(\frac{v_w}{27}\right)^2 \exp\left(-\frac{h}{1000}\right) + s_2 \exp\left(-\frac{h}{1500}\right) + S\exp\left(-\frac{h}{100}\right) \quad (1)$$

where v_w is the high altitude wind speed, s_1 $(\sim 10^{-53})$ and s_2 $(\sim 10^{-16})$ are the site and time dependent weights and S is the scaling factor for surface turbulence. C_n^2 has a squared dependence on the wind speed.

Setting the operating bandwidth sufficiently high as compared to the Greenwood frequency, f_G is an important step in the design of adaptive optics systems.[10] Operational bandwidth is governed by the servolag error which is the time delay between wavefront sensing and wavefront correction. It includes the photon integration time, readout timescales of the detector at the sensor

[1]Indian Institute of Astrophysics, Koramangala, Bangalore 560034, India.
[2]Advanced Optical Imaging Group, School of Physics, University College Dublin, Dublin, Ireland.
*brp@iiap.res.in

end and wavefront sensing and reconstruction times. Readout timescale is a detector specification and the wavefront sensing time depends on the number of degrees of freedom in wavefront corrector (in general also equal to the number of subapertures of Shack Hartmann wavefront sensor) and wavefront reconstruction algorithm. Optimum integration time is a result of trade-off between measurement error due to limited photon flux and the bandwidth of operation.[1] The servo lag error can be reduced by predicting the wavefront which is arriving at the instant of wavefront correction using a reasonable assumption that the wavefronts are correlated within the encountered time delays.[11,12] The prediction accuracy strongly depends on the Fried's parameter and wind speed. Analysing the reported r_0 measurements at the Oukaimeden site, it can be noted that within 0.5 hrs, r_0 fluctuates with a standard deviation of 1.33 cm.[13] The RMS variability of wind velocity is 0.5 m/s within 10 s as reported earlier by two independent surveys at two different sites[3,14] and within 10 minutes it can fluctuate about 2–3 m/s. A real-time variability of these atmospheric parameters affects the prediction metrics significantly.[12] Hence a real-time monitoring of the wind velocity is an inevitable requirement in adaptive optics.

Advanced Doppler LIDAR techniques are used for wind profile measurement during site testing.[15] Wind sensors based on the calculation of time-lagged covariance function of the amplitude scintillations for a system consisting of a source and two equal aperture detectors was suggested earlier.[16] A smart speckle correlation technique based on image binarization improved the quality of wind velocity measurements.[17] Recently Banakh and Marakasov[18] retrieved wind profile from turbulent plane-wave intensity fluctuations. All of these techniques require additional design, cost, and maintenance and observatory space. Shack Hartmann wavefront sensor[19] which measures the atmospherically induced distortions can be used for this purpose instead. It was used earlier to characterize the form of the structure function of phase fluctuations and quantify the deviations from Kolmogorov phase spectrum.[20,21] Methods of recovering r_0 values in real time from wavefront slope measurements made by the Shack Hartmann wavefront sensor and image processing exist in the literature.[22] Schock and Spillar[23] used Shack Hartmann wavefront sensor data to measure wind speed through the identification of maxima on the convective autocorrelation function using the fact that each layer creates a peak in the autocorrelation of the wavefront sensor data. Using the wavefront sensor data, on-line characterization of turbulence parameters was performed by Fusco.[24]

A technique was proposed to determine the magnitude and direction of wind velocity from wavefronts reconstructed using the Shack Hartmann wavefront sensor slope data. Assuming Taylor's frozen in turbulence approximation,[25] phase screens are numerically generated by a linear superposition of wavefront distortions at different layers. Translating compact disk casing is used to emulate dynamic turbulence in the laboratory.[26] The wind velocity measurement technique is implemented on phase screens simulated using the Fourier technique,[27–29] covariance matrix based on von Karman spectrum,[30] Kolmogorov spectrum based Zernike covariance matrix[31,32] and experimentally obtained data. The proposed technique involves the calculation of temporal correlation maps and identification of correlation peaks to arrive at wind speed and direction. This wind measurement technique is sufficiently accurate and helps in minimizing errors associated with bandwidth control. However, this wind measurement method requires optimization of certain parameters. Correlation maps are made using a small portion of the phase screen in the time series data from the sensor. The size of the portion picked up from the large phase screen controls wind speed estimation accuracy to a great extent. If a large portion is selected, it takes longer time for computation of temporal correlations. Selecting a very small portion would temporally decorrelate them very soon. Optimizing the number of temporal phase screens (number of realizations) used for estimation of wind speed is also crucial in reducing the time of computation. The dependence on these two parameters is analysed and optimized for large wavefronts.

2 Simulating Temporally Evolving Turbulence

Simulation of phase screens emulating atmospheric turbulence helps in testing and modelling of device parameters in adaptive optics. To test the developed wind velocity measurement technique, temporally evolving phase screens (assuming Taylor's frozen field hypothesis) are simulated using three different methods,

Method 1: Translating wind model applied to phase screens following Kolmogorov spectrum derived from Zernike covariance matrix calculations.

Method 2: Phase screens derived from the temporal covariance matrix following von Karman atmospheric turbulence spectrum.

Method 3: Simulation of large phase screens using Fourier technique.

2.1 *Method 1*

Phase screens, $\phi(x, y)$ as a linear combination of Zernike polynomials, $Z_i(x, y)$ can be simulated by calculating Zernike moments, a_i ('a' in vectorial form) following Kolmogorov spatial statistics[31] such that,

$$a = Cb$$
$$\phi(x, y) = \sum_{i=1}^{M} a_i Z_i(x, y) \tag{2}$$

where 'b' is a column vector containing pseudo random numbers with zero mean and unit variance, 'M' is the number of Zernike polynomials used to represent a phase screen ($M = 180$ in our case), C is the Cholesky factor of the covariance matrix of Zernike moments, $<a_i a_j>$.

$$< a_i a_j > = 0.0072\pi^{8/3}\delta_{m_i m_j}(-1)^{(n_i+n_j-2m_i)/2}\left(\frac{D}{r_0}\right)^{5/3}\left\{(n_i+1)(n_j+1)\right\}^{1/2} \times \frac{\Gamma(14/3)\Gamma\left[(n_i+n_j-5/3)/2\right]}{\Gamma\left[(n_i-n_j+17/3)/2\right]\Gamma\left[(n_i-n_j+17/3)/2\right]\Gamma\left[(n_i+n_j-23/3)/2\right]} \tag{3}$$

where n_i and m_i are radial and azimuthal indices of Zernike polynomials, D is the telescope aperture diameter. Lower order Zernike moments (representing piston and tilt) are not used for simulation of phase screens. Adopting the wind model used in the dynamic turbulence generator of Hu,[33] temporally evolving turbulence is simulated.

2.2 *Method 2*

Phase covariance matrix of $\phi(\vec{X}, t)$ for the wavefront propagation through atmospheric turbulence following von Karman power spectrum is given by,[30]

$$\gamma_\phi(\rho) = \frac{0.033(2\pi)^5 C_n^2 z\left(L_0/4\pi\right)^{5/6} K_{5/6}\rho^{11/6}}{\lambda^2 L_0 \Gamma(11/6)} \tag{4}$$

where $\rho = \left|\vec{X} - \vec{X}' - v(t - t')\right|$. Here, z is the thickness of an atmospheric turbulence layer; L_0 is the outer scale of turbulence; $K_{5/6}$ is the modified Bessel function of the second kind; v is the wind speed, $\vec{X}$, $\vec{X}'$ are the grid points on the phase screen; and t, t' represent time. By changing z, C_n^2 and v, multiple layers can be simulated and superposed.

2.3 *Method 3*

It is possible to rapidly generate large random phase screens based on fast Fourier transform technique.[28] The inaccuracies in this technique are reduced by using a sub-harmonic method suggested by Lane[34] and later modified by Johansson and Gavel.[27] The simplest phase screen following von Karman spectrum with a grid dimension of $N_x \times N_y$ pixels is given by,

$$\phi(x,y) = \sum_{X=-N_x/2}^{N_x/2-1}\sum_{Y=-N_y/2}^{N_y/2-1} h(X,Y) f(X,Y) \times \exp\left\{2\pi i\left(\frac{Xx}{N_x}\right) + \frac{Yy}{N_y}\right\} \tag{5}$$

where $f(X, Y)$ is the square root of the turbulence power spectrum defined,

$$f(X,Y) = \frac{2\pi}{\sqrt{G_x G_y}}\sqrt{0.00058}\; r_0^{-5/6} \times \left[\left(\frac{X}{G_x}\right)^2 + \left(\frac{Y}{G_y}\right)^2 + \frac{1}{L_0^2}\right]^{-11/12} \tag{6}$$

Here $h(X,Y)$ represents the elements of a Hermitian matrix containing white noise, G_x and G_y represent the physical dimension of the phase screen. In order to generate temporal evolution, a small portion of the simulated large wavefront is selected and moved across.

Atmospheric turbulence is simulated by superposing temporally evolving wavefronts at different altitudes. In our study, a seven layered model of turbulence is used. The whole of turbulence column is divided into seven different layers. Since wind velocity is altitude dependent a good modelling of the vertical wind velocity profile is essential

for simulation of wavefronts closer to atmospheric turbulence. It is in general approximated with a Gaussian model.[10] Here, the wind model was approximated to the measurement results of Gentry[15] to simulate temporal turbulence. An example of the wind profile used in our simulations is shown in Table 1. Since the direction does not change significantly within the decorrelation time, the layers are moved in a predefined direction for modelling.

The superposition of layers although seems straight forward, its complexity grows with the number of layers and also when velocity has to be represented more accurately.

Since different layers move at different velocities at a given instant, there might be a need to move the phase screen at some of the layers by subpixel amounts for better accuracy. Statistical interpolation was performed in order to obtain subpixel shift of phase screens for arbitrary velocities.[35] Statistical method has an edge over bilinear interpolation since it retains the spatial statistics of atmospheric turbulence even after interpolation.[36]

Temporally evolving phase screens using single as well as multilayer models of turbulence are shown in Figs. 1 and 2. The correlation coefficient reduces with increasing time as shown in Fig. 3.

Table 1: Atmospheric layers used to simulate temporal evolution of turbulence.[15]

Layer	Altitude (km)	Wind speed (m/s)
1	2.5	5
2	5.0	10
3	7.5	15
4	10.0	20
5	12.5	15
6	15.0	10
7	17.5	5

2.4 *Obtaining phase screens in the lab*

Wavefront sensor data was obtained in the laboratory using a translating CD casing[26] as shown in Fig. 4. The sensor is a Diffractive Optical Lens (DOL) based Shack Hartmann on a Spatial Light Modulator (Model LC 2002 from HOLOEYE). The locations of focal spots are identified by performing centroiding of the spots using the iteratively weighted center of gravity algorithm (base weighting function is a Gaussian intensity distribution). Vector matrix multiply method is used to reconstruct wavefronts from the measured slope values. A 633 nm He-Ne laser was used as the light source. The DOL based sensor contained 144 (12 × 12) subapertures (lenses). 52 × 52 pixels on SLM were used to make a single subaperture. The CD case (1.35 mm thick) was translated (upto 3.5 mm in steps of 10 m) horizontally in the direction perpendicular to the propagation of the light beam to emulate the moving atmospheric layer.

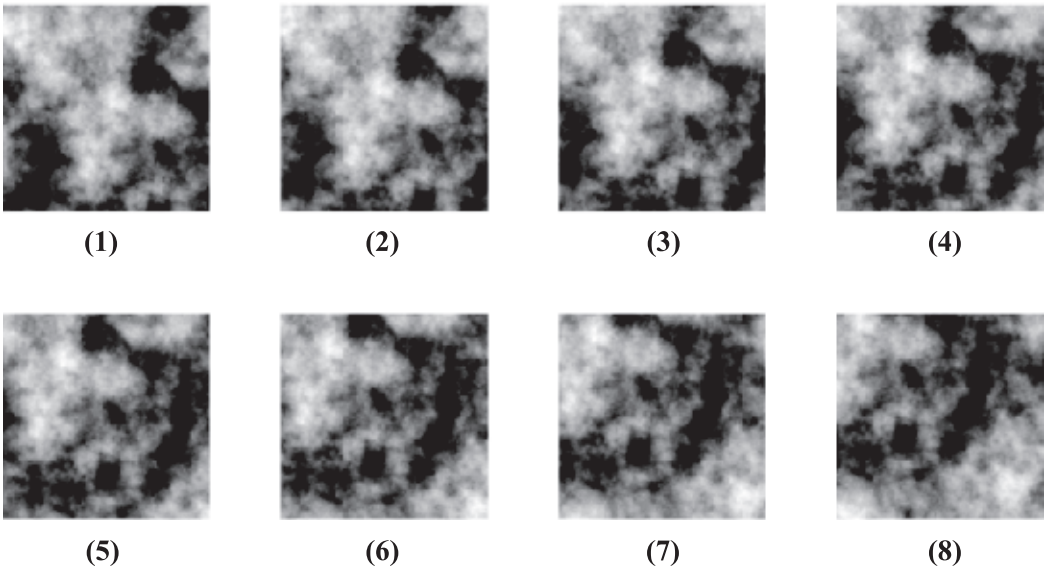

Figure 1: Evolving phase screens (1–8) simulated using Fourier technique by using a single layer with average wind speed = 8 m/s. Phase screen resolution: 200 × 200 pixels; r_0 = 0.1 m; Phase screen dimension: 2 × 2 m^2; L_0 = 12 m. Adjacent phase screens shown above are 63% correlated and temporally separated by 10 ms.

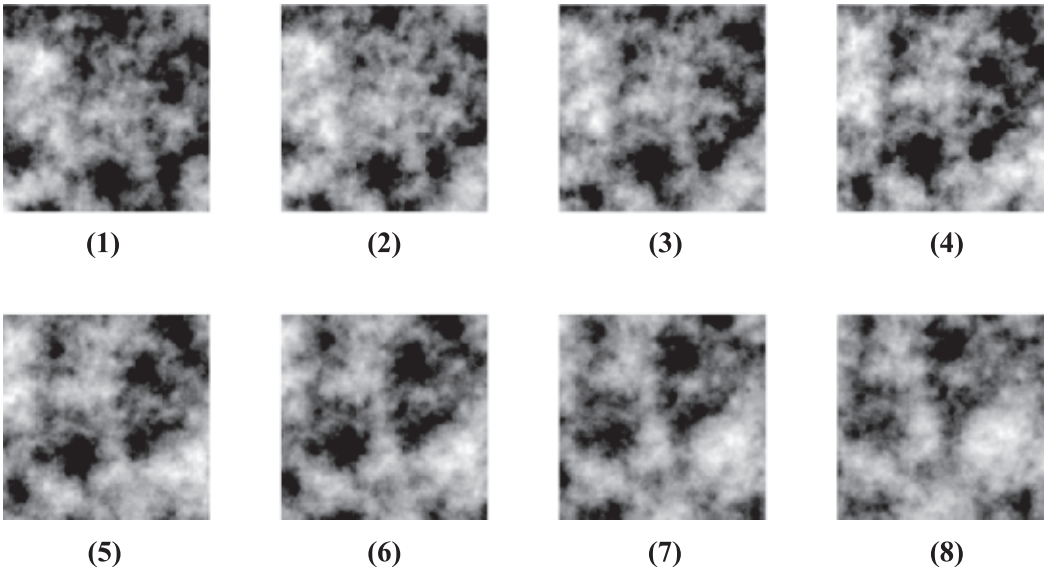

Figure 2: Evolving phase screens (1–8) simulated using Fourier technique by addition of 7 layers from the model described in Table 1. Mean wind speed = 10 m/s; Phase screen resolution: 200 × 200 pixels; r_0 = 0.1 m; Phase screen dimension: 2 × 2 m^2; L_0 = 20 m. Adjacent phase screens shown above are 65% correlated and temporally separated by 10 ms.

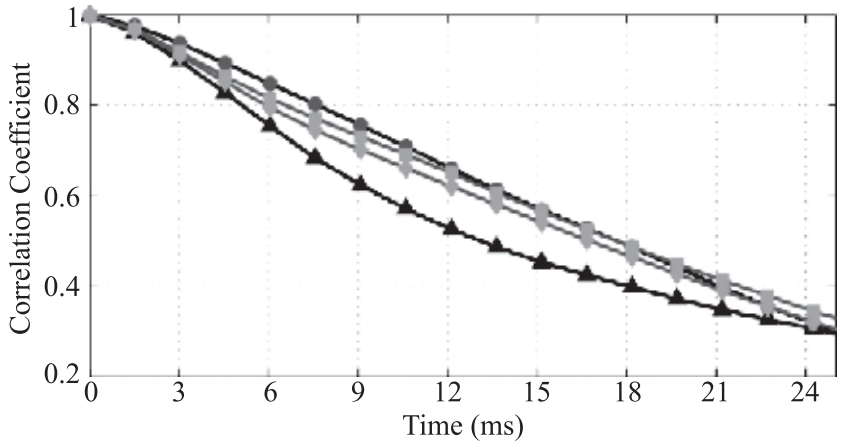

Figure 3: Drop in the correlation of subsequent screens with respect to the first phase screen—4 different temporal realizations.

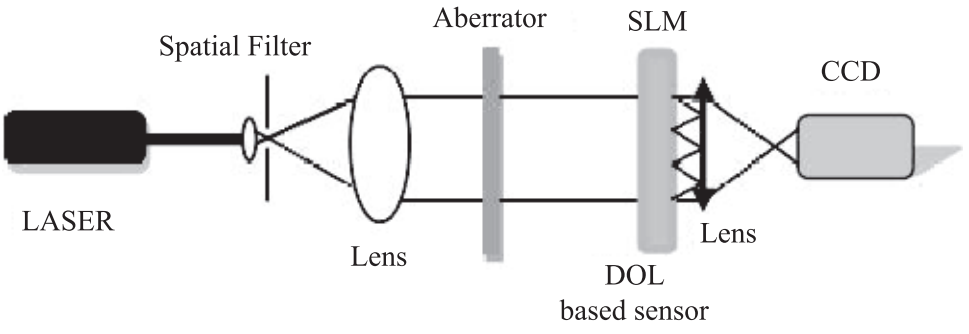

Figure 4: Experimental setup to obtain wavefront data.

3 The Proposed Method

3.1 *Forming data cubes*

The evolving turbulence phase screens are arranged in a sequence and are stored as three-dimensional arrays called data cubes. The temporal sequence is hence represented as A_{ij}^{k} where i; j are the spatial indices representing the pixels of the phase screen and k is the temporal index ($1 \le i \le N_x$, $1 \le j \le N_y$, $1 \le k \le T$, where 'T' phase screens are well within the decorrelation time). Formation of the data cubes helps in keeping track of the wavefront decorrelation time and hence the number of phase screens to be used for data analysis.

3.2 *Formation of correlation maps*

Formation of the correlation maps is the most important step in this method. A small portion A^1 (called seed phase screen of size $\Re \times \Re^1$ pixels: $\Re << N_x$, $\Re^1 << N_y$) is selected close to the center of the first phase screen A_{ij}^{1} (of size $N_x \times N_y$ pixels) in the time sequence, A_{ij}^{k}. This newly formed seed phase screen is compared against arrays of same size, $A_{gg'}^{k}$, corresponding to all the positions where mapping is possible. Here, $A_{gg'}^{k}$ represent arrays of size $\Re \times \Re^1$ pixels formed from A_{ij}^{k} such that $(1+g) \le i \le (\Re + g)$, $(1+g') \le j \le (\Re^1 + g')$ where, $0 \le g \le N_x - \Re$ and $0 \le g' \le N_y - \Re^1$). The metric used for comparison is the correlation coefficient, $\chi_{gg'}^{k}$

$$\chi_{gg'}^{k} = \frac{E\left[(A^1 - \mu^1)(A_{gg'}^{k} - \mu_{gg'}^{k})\right]}{\sigma^1 \sigma_{gg'}^{k}} \qquad (7)$$

where, μ and σ correspond to mean and standard deviation respectively. The range of values that g and g' can assume clearly indicates that there can be $(N_x - \Re + 1) \times (N_y - \Re^1 + 1)$ values of $\chi_{gg'}^{k}$ for a given 'k' and hence written in matrix format, χ^k.

χ^k's for different k's are formed and stored in a data cube as described earlier. This correlation map data cube is used for measurement and analysis of wind speed and direction. The phase screen data cube changes with time and hence the seed phase screen and the correlation map data cube.

3.3 *Wind velocity estimation*

The peak in the 'k'th ($1 \le k \le T$) correlation map (χ^k) is identified as a first step. A pair of phase screens (for example, χ^1–χ^3) is chosen from the correlation map data cube. A vector is formed by joining the positions of the peaks in the two correlation maps. The length of this vector is calculated. Wind speed is estimated by taking the ratio of the distance travelled by the correlation peak and the temporal separation between the frames of interest ($2 \times \Delta t_{int}$ in the case of χ^1–χ^3). The measured wind speed value has meaning only if the measurement is performed using a pair of phase screens well correlated in time. In the case of a telescope of diameter $D = 2$ m, $v_w = 10$ m/s, the wavefront decorrelation time is $\tau_d = D/v_w = 0.2$ s. Therefore only those phase screens which are separated temporally by less than 0.2 s can form pairs. The estimated wind speed can be compared and calibrated against measurements made using some other instruments.

The position of the correlation peak is tracked within the wavefront decorrelation time and hence the wind direction is arrived. The estimation of direction helps in completely determining the characteristics of atmospheric wind speed. Sudden jumps in the traced path are treated as errors and those realizations are excluded.

There is certainly a chance that the identified peak in the correlation maps may not be the correct one. This can lead to large errors. To overcome these problems, the following techniques are used.

3.4 *Validation of the estimated wind speed*

3.4.1 Probability density function: Effective wind speed: The wind speed is estimated several number of times using multiple realizations possible from the data within the decorrelation time (for a decorrelation time of 0.2 s and frame rate of 5 ms, there are 40 phase screens in number which means that there are $^{40}C_2$[=780] possible pairs). The probability density function of the measured wind speed is obtained. The peak in the probability density function is identified as the effective wind speed. Fitting the obtained probability density function with either a Gaussian or an appropriately defined function would improve the accuracy of the method.

3.4.2 Selective reduction: Realization selection is one of the most commonly used techniques for data filtering. In this method, wind speed (V_i) is estimated using all possible realizations (i). The mean of V_i is calculated, V_i^{mean}. A new data set, V_j is selected from V_i such that, $V_i^{mean} - eV_i^{mean} \le V_j \le V_i^{mean} + eV_i^{mean}$, $\forall j$. The factor 'e' decides the size of the allowed error window. Mean of V_j becomes the estimated wind speed from the newly formed data set. This process can be repeated again and again and hence is an iterative process.

3.4.3 Hybrid method: In the hybrid technique, both the above methods are put into practice. The

peak in the probability density function is identified as the first step. This value is used in the first iteration of the selective reduction technique. This method helps in identifying the most likely value from the realizations and also accurately estimates it.

3.5 *Single-layer model*

Temporally evolving phase screens (100 in number in one sequence; 200×200 pixels each; single layer model) of area 2×2 m^2 were simulated using the fast Fourier technique where $L_0 = 12$ m, $r_0 = 0.1$ m with integration time, $t_{int} = 5$ ms. Since 1 pixel of the phase screen is equivalent to 10 mm on the aperture, effective wind speed $v_{eff} = 2$ m/s when adjacent frames are formed by moving 1 pixel with respect to each other. Similarly, for different magnitudes of pixel shift from frame to frame, the expected mean velocity is given in Table 2. Wind speed was estimated using the hybrid method and tabulated.

100 realizations were used in each of the 10 independent temporal sequences where wind speed was estimated. Similar results were obtained by applying the technique on phase screens simulated using Method 1 and Method 2. The motion of CD case was detected within 10% error.

3.6 *Multiple layer model*

Consider the case of a more realistic multi-layer model of atmospheric turbulence. The parameters used for modelling are the same as that used for single layer model with a difference that 7 layers are superposed using the velocity model in Table 1. Since the direction of the wind at different layers does not change rapidly[15] (within the decorrelation time), all the layers were moved in a single direction. The expected and obtained wind speed measurement results are shown in Table 3.

Table 2: Single layer turbulence model: Wind velocity measurement.

Pixels shifted per frame	Expected mean wind speed (m/s)	Estimated by the proposed method (m/s)
1	2	2.03
2	4	3.98
3	6	6.36
4	8	8.24
5	10	10.18
6	12	11.88
7	14	13.58
8	16	15.80

Table 3: Multilayered turbulence model: Wind velocity measurement.

Expected mean, wind speed (m/s)	Estimated by the proposed technique (m/s)
8	8.23
10	9.61
12	11.55

Figure 5: Single layer model: Wind direction measurement by tracing the peak in the correlation maps data cube.

Figure 6: Multilayer model: Wind direction measurement by tracing the peak in the correlation maps data cube.

3.7 *Estimating wind direction*

The measurement results of the direction of the wind in the case of single and multilayered models are shown in Figs. 5, 6, and 7. It can be noted that due to mixture of layers, the detection of wind direction is more complicated and involves large errors when compared to a single layered model. The case of horizontally translating CD casing is shown in Fig. 8.

3.8 *Size of seed phase screen: Relation to estimation accuracy*

Optimizing the size of the seed phase screen to be selected from the larger one plays an important role in increasing the accuracy of wind speed estimation. Here the percentage accuracy of estimation is defined as,

Figure 7: Multilayer model: Wind direction measurement by tracing the peak in the correlation maps data cube.

Figure 8: Wind direction measurement in the case of horizontally translating aberrator plate across the beam path.

$$\tilde{a} = \left[1 - \frac{|\text{Estimated value} - \text{Actual value}|}{\text{Actual value}}\right] \times 100 \quad (8)$$

Relative size of the seed phase screen (of size 's × s' pixels) with respect to A^1_{ij} (of size '$N \times N$', where $N = N_x = N_y$) is given by $[(s/N) \times 100]$. Choosing a too small or very large seed phase screen would not yield good results. Optimum size of the seed phase screen was found to be 48 × 48 under the assumed conditions as shown in Fig. 9.

3.9 *Optimizing the number of realizations*

The proposed wind speed estimation technique makes use of phase screen pairs. Hence, the timescale of separation between the phase screen pairs and the correlation between them is not indifferent to the obtained accuracies in the measurement as shown in Fig. 10. The number of required realizations needs to be optimized for accurate and quick estimation of wind speed. Increasing the number of realizations although increases the accuracy of wind velocity determination, it is important to note that within the decor-relation time there are a limited number of possible realizations. Also, it may not be necessary to always exhaust all the realizations since it may lead to saturation as shown in Fig. 11 (for a single simulated temporal sequence). The selective reduction technique

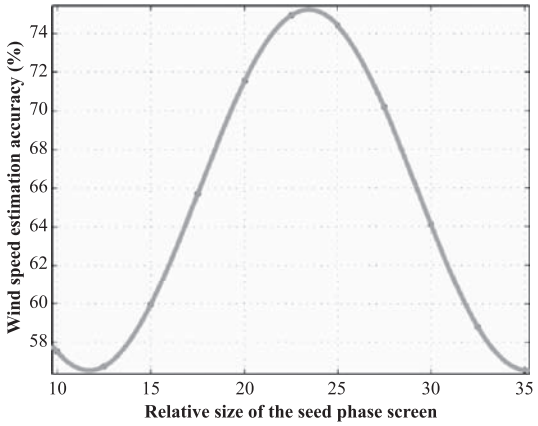

Figure 9: Wind speed estimation accuracy—Relation to size of the seed phase screen. Applied to 7 layer model of turbulence with mean wind speed 10 m/s, $r_0 = 0.1$ m, $L_0 = 10$ km, D = 2 m, 200 × 200 pixels.

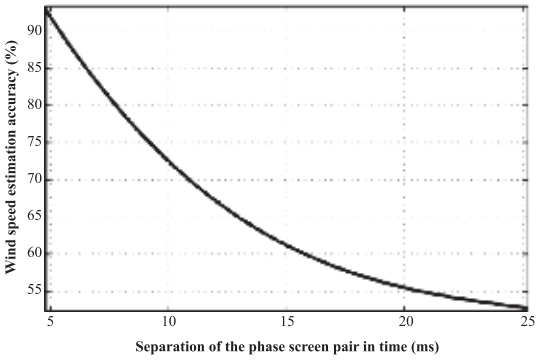

Figure 10: Wind measurement accuracy—dependence on temporal separation of phase screen pairs.

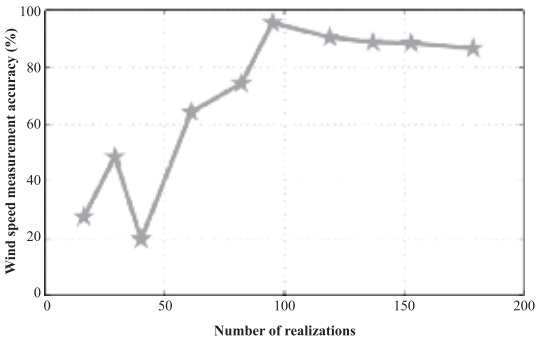

Figure 11: Dependence of accuracy on the number of realizations used for wind speed estimation—using the selective reduction technique (1 iteration), applied to a single temporal sequence.

and the hybrid technique involve large number of realizations (due to the fact that selective reduction reduces the realizations by a factor of 3 after a single iteration), but arrive at a more accurate value of wind speed. The probability density function based technique is less accurate but is not as much time consuming.

4 Experimental Evaluation: Wind Speed Measurement Using SHWS

Demonstration of the experimental validation of the cross-correlation method based on peak identification to estimate the transverse wind speed using a phase plate and a SHWS is presented in this section. The cross-correlation peak occupies only a few discrete pixels and hence to identify the location of the peak, interpolation techniques are adopted.

The following section describes the optical arrangement employed to obtain the SHWS data experimentally. Next, the results of the calibration of the phase plate that was used to simulate turbulence in the laboratory are presented. The wavefront reconstruction procedure in the SHWS, various methods used for wind speed estimation from the calculated cross correlation function and different peak identification techniques are described in the subsequent sections. Results of the analysis performed on the experimentally obtained data and conclusions are presented followed in the later section.

4.1 *Wavefront sensor data*

The experimental setup used to obtain the wavefront sensor data is shown in Fig. 12. A 15 mW Melles Griot He-Ne laser with a wavelength of = 632.8 nm was used as the source of light. The laser beam was spatially filtered using a 40x objective lens and 5 μm pinhole. It is then collimated using a doublet lens (CL) of focal length f = 15 cm. The collimated beam was allowed to be incident on a phase plate. After passing through the phase plate, the outcoming distorted beam was sensed using a SHWS. The SHWS was made up of a microlens array and a CCD camera placed at the focal plane of the lenslet array. A neutral density filter (NDF) was placed in front of the laser source so as to control the intensity of light falling on the CCD camera. The microlens array is from Flexible Optical BV (OKO technologies) and is of size 2×2 cm^2 consisting of an array of 100×100 microlenses with 200 μm pitch. The focal length of the microlenses is 4 cm. A monochrome progressive scan CCD camera (Pulnix TM 1325-CL) placed at the focal plane of the microlens array captures the spot pattern. Initial characterization results have been presented earlier.[37]

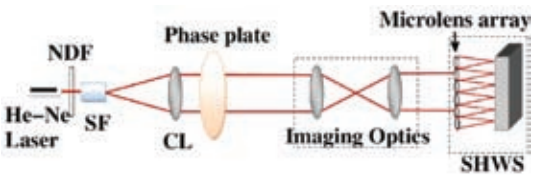

Figure 12: Experimental setup to obtain wavefront sensor data.

The phase plate that was used in our experiment is a pseudo random phase screen designed by Lexitek, with the optical path difference defined over an annular region of a 4096 4096 array. The phase map was made with a Near-Index-MatchTM optic. The Fried parameter of the phase plate is 400 μm at a wavelength of 633 nm. The phase map design of the phase plate assumes the Kolmogorov model of atmospheric turbulence.

Since the active detector area is 8.4×6.7 mm^2, it is also the useful optical beam size. Hence, only a small portion of the phase screen is seen by the SHWS at a given instant. This corresponds to a smaller portion of the microlens array (~42×33 lenses).

The dynamic behaviour of atmospheric turbulence was realized in the laboratory by mounting the phase plate on a rotary stage and driving it with the help of a calibrated motor. The rotation speed of the phase screen is varied to achieve different velocities. The experimental conditions correspond to a single layer atmospheric turbulence model with a fixed wind speed, where Taylor frozen in turbulence hypothesis is completely valid.

The background noise caused because of stray light can be effectively eliminated by capturing a background image in the absence of microlens array and phase plate (see Fig. 12). A reference focal spot pattern was taken by placing the microlens array in the absence of phase plate in the beam path. The background image is subtracted from the reference image and the spot pattern image taken with the phase plate in the beam path. The resultant images are then used for reconstructing the phase of the incident wavefronts.

4.2 *Phase plate calibration*

4.2.1 Phase plate to SHWS compatibility: It is important to design the wavefront sensing experiment in such a way that the SHWS and the wavefront sensing algorithm can efficiently detect the distortions introduced by the phase plate. The coherence length of the phase plate defined by the Fried parameter, r_0 in our case is 400 μm. As the number of microlenses used for wavefront

sensing is increased for a given area, the spatial sampling and spatial resolution are increased. Also, since the pitch of the microlens array used for wavefront sensing is 200 μm, the sampling is being done at double the spatial frequency of phase plate distortions, given the unit magnification employed in the imaging optics (see Fig. 12).

4.2.2 Phase plate speed calibration: The phase plate is mounted on a rotary stage assembly; the movement is steered by a motor that is regulated using a Lexitek stepper controller. The controller, capable of standalone operation was used for changing the rotation speed. The command MVS sets the move speed and is quantized to multiples of 12.5 pulses per second (pps). A simple calibration procedure was carried out to measure the speed of the phase plate and test its linearity with changing move speed (MVS). The time taken for a single rotation of the phase plate was measured for different rotation speeds starting from 12.5 pps to 400 pps (see Table 4).

Since the region-of-interest (ROI) occupies a very small area, *dA* (see Fig. 13), for the calculation of the speed, it is approximated that the distance moved by the ROI in a single rotation is equal to the perimeter of the dotted circle in Fig. 13, which has a radius, *r* that is equal to the length of the line joining the center of the phase plate and the center of the ROI. In our case, $r = 30$ mm and hence a one rotation distance of 188.4 mm. Measurement of the time taken for a single rotation gives the speed of movement of the phase screen across the SHWS. The calibration plot of the speed of the rotary stage motor for different MVS is shown in Fig. 14.

Table 4: Speed calibration of the rotary stage motor.

MVS	Time for one rotation (s)	Speed (in mm/s)
12.5	767.98	0.245
25	384.44	0.490
37	255.97	0.736
50	191.51	0.984
62.5	153.61	1.226
75.0	127.83	1.474
87.5	109.78	1.716
100.0	95.88	1.965
112.5	85.47	2.204
125.0	77.30	2.437
137.5	69.63	2.706
150.0	63.91	2.948
200.0	47.88	3.935
250.0	38.37	4.910
300.0	32.15	5.860
400.0	24.01	7.847

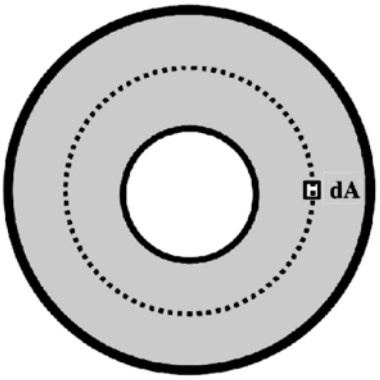

Figure 13: Small area approximation: Distance travelled in one rotation is equal to the perimeter of the dotted circle.

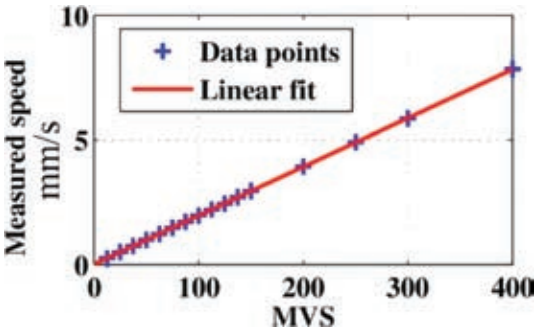

Figure 14: Calibration of the rotary stage speed with the MVS function in the motor controller.

4.2.3 Scaling to astronomical dimensions: In order to check the suitability and applicability of the turbulence simulated using the phase plate and performing a numerical evaluation of the wind speed measurement techniques, it would be appropriate to scale the simulated turbulence to astronomical dimensions.

Comparing the case of a telescope situated at a site where $r_0 = 25$ cm with the phase plate $r_0 = 400$ μm, the beam downscaling in our experiment can be calculated to be 625:1. Thus, with the ROI being of dimensions 5×5 mm^2 (25×25 microlenses used for sensing), the corresponding telescope aperture size would be of diameter 3.125 m.

From Table 4, it can be noted that with MVS = 400, the effective translation velocity of the phase plate across the detector is 7.847 mm/s. In realistic case, this would correspond to 4.9 m/s. Employing a faster CCD, it would be possible to

analyse greater wind speeds (i.e., phase plate can be moved with greater MVS).

4.3 *Wavefront reconstruction*

The SHWS spot pattern images were captured at a rate of 30 frames per second. A single frame captured by the CCD camera is shown in Fig. 15. Using sequential data acquisition, a sequence of 100 images, with well-defined time separation, were captured for a given rotation speed, and were arranged in the form of a data cube.

In order to choose a correct region-of-interest (ROI), a simple peak search algorithm from the image center to locate the central SHWS spot was adopted. The ROI was then selected appropriately so that a 25 × 25 SHWS spot pattern image is obtained. Once the background noise on the images is removed, centroiding is performed on individual spots to locate the centroids. At good light conditions (see Fig. 15), the simple center of gravity algorithm performs a decent job and hence it was preferred to be used for centroiding.[38] The details of this algorithm are discussed in later sections, with regard to the detection of the cross-correlation peak.

The difference in the centroid locations of the spot pattern and reference spot pattern gives the local slopes of the wavefront distortions across each microlens of the lenslet array. These local slopes from the wavefront sensor are used to reconstruct the wavefront shape. The iterative least square method was used for wavefront reconstruction.[39] A few samples of the phase maps that were obtained after applying the wavefront reconstruction algorithms are shown in Fig. 16.

The obtained wavefront phase maps are 25 × 25 sized matrices, each point on the array containing the relative phase value. Bilinear interpolation was used to re-size these phase maps to 100 × 100 sized matrices and is saved in the form of a data cube. The slope data and reconstructed wavefront phase data obtained in this manner was analysed using different wind velocity measurement techniques to calculate the speed and compared with the known speed. The various methods employed in our work and the results of the wind velocity measurement are discussed in the following sections.

Figure 15: A sample spot pattern image captured by the SHWS camera with the phase plate in the beam path.

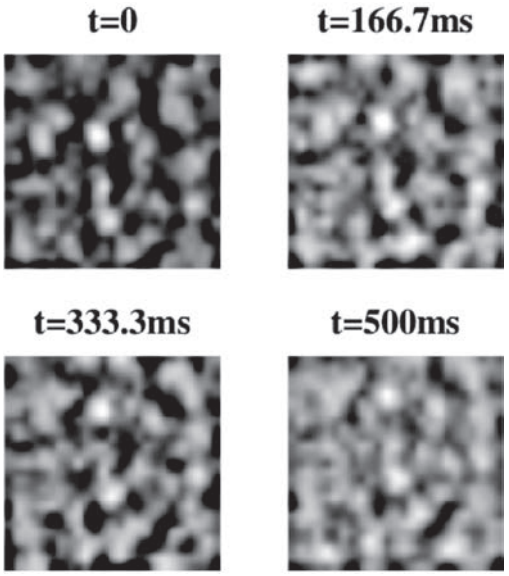

Figure 16: Gray scale maps of the reconstructed phase with MVS = 100.

4.4 *Temporal correlation coefficient*

The correlation coefficient χ_k^1, can be used as a metric for comparison of time evolving reconstructed wavefronts. Here, 'k' represents the time index and '1' in the superscript suggests that the comparison is always made with the first wavefront in the time sequence.

$$\chi_k^1 = \frac{E\left[(A^1 - \mu^1)(A_k - \mu_k)\right]}{\sigma^1 \sigma^k} \tag{9}$$

where, μ and σ correspond to mean and standard deviation respectively, and $1 \le k \le 100$.

Fig. 17 shows a comparison of the temporal correlation coefficient for different MVS. The decay of the temporal correlation coefficient is slower in the case of MVS = 12.5 and very fast in the case of MVS = 100. Also, it should be noted that the decay rate of the temporal correlation coefficient increases with increasing move speed until the correlation coefficient drops below a value of

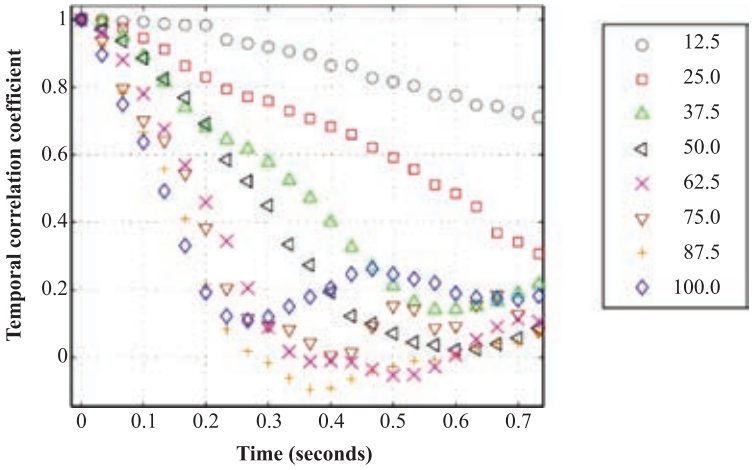

Figure 17: The decay of the correlation coefficient with time for different MVS.

0.2, after which the behaviour is random since the later wavefronts are completely different from the first wavefront (especially for MVS beyond 62.5 as shown in Fig. 17).

4.5 *Methods to estimate wind speed from SHWS*

Fig. 18 shows the normalized time-lagged auto-covariance and cross-covariance functions as described by Wang.[16] The horizontal axis stands for the time co-ordinate. The different parameters appeared in the plot and different wind velocity measurement techniques are described below, t_p-time delay at the peak of the cross covariance curve; t_c-cross over time delay of the auto covariance and cross covariance curves; t_f-width of the auto covariance curve at half power point; and S_0-slope of the cross co-variance curve at zero time delay.

4.5.1 Peak technique:

$$V_p \sim \frac{\rho}{t_p} \tag{10}$$

where ρ is the separation between the subapertures of the SHWS under consideration for calculation of auto covariance and cross-covariance.

4.5.2 Slope technique:

$$V_s \sim S_0 \tag{11}$$

The wind speed is estimated after calculating the slope near zero delay of the normalized time-lagged covariance of the measured signals in logarithmic scales.[40]

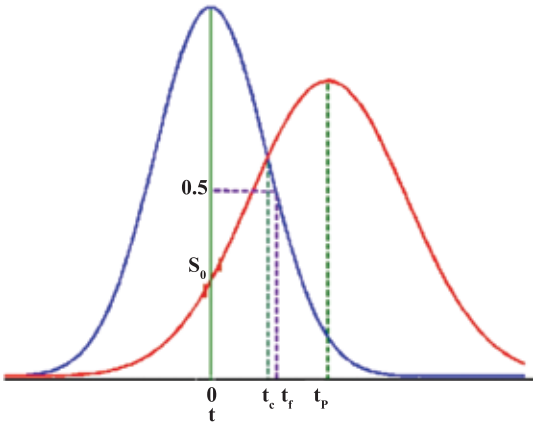

Figure 18: Auto-covariance (blue colored curve) and cross-covariance (red colored curve) functions.

4.5.3 Frequency technique:

$$V_f \sim \frac{1}{t_f} \tag{12}$$

The above expression also suggests that the width of the autocovariance function has information about the wind speed.[41]

4.5.4 Briggs technique:

$$V_b = \frac{\rho}{2t_c} \tag{13}$$

Briggs et al.[42] developed a method for evaluating wind speed using spaced receivers. It was shown that the cross over time delay between the

autocovariance and cross covariance is inversely proportional to wind speed.

Here, a closer look was taken at the peak identification technique and different algorithms were compared.

4.6 *Calculation of the 2D cross correlation matrix*

The cross-correlation matrix of two phase maps, P_1 and P_2 (of dimension 100×100 each separated by a time interval, ΔT), is obtained by spatially shifting (in discrete steps) one of the phase maps (say, P_1) to all possible locations and calculating its correlation coefficient with the non-shifted phase map (P_2) as described in Eq. 9.

4.6.1 Peak detection techniques: Since the number of active pixels that are near the peak of the autocorrelation function, and their contribution to the accurate peak detection is generally small, a peak detection technique is required to accurately measure sub-pixel shifts of the cross-correlation peak. The identification of the auto-correlation peak and the cross-correlation peak can be done either using different interpolation or centroiding techniques. In this work, two interpolation techniques, namely Gaussian and Parabolic are used. Also, the performance of three centroiding algorithms-center of gravity (CoG), weighted center of gravity (WCoG) and iteratively weighted center of gravity (IWCoG) is tested and compared with the interpolation techniques.

4.6.2 Three-point Gaussian interpolant: The pixel location of the peak in the two dimensional correlation map is initially identified. Two points on either side of the peak value along 'x' axis are taken and a Gaussian interpolation of three adjacent sample points is performed.

In order to use the Gaussian interpolator of the form,

$$f_g(k) = A\exp\left[-\frac{(x-x_0)^2}{2\sigma^2}\right] \tag{14}$$

'x_0', the location of the Gaussian peak can be computed from the following expression:

$$x_0 = \frac{1}{2}\left[\frac{R'-L'}{2M'-R'-L'}\right] \tag{15}$$

$$\sigma^2 = \frac{1}{2M'-R'-L'} \tag{16}$$

$$\log_{10} A = M' + \frac{x_0^2}{2\sigma^2} \tag{17}$$

The primed quantities, R', M', L' are the logarithmic values of $f_G(1)$, $f_G(0)$ and $f_G(-1)$ respectively.

It can be observed that the shape of the cross-correlation function does not maintain a Gaussian shape at all times as can be seen in Fig. 19. Hence, better peak detection techniques are necessary.

4.6.3 Three-point parabolic interpolator: To obtain a resultant fit of the form,

$$f_p(k) = a(k-p)^2 + b \tag{18}$$

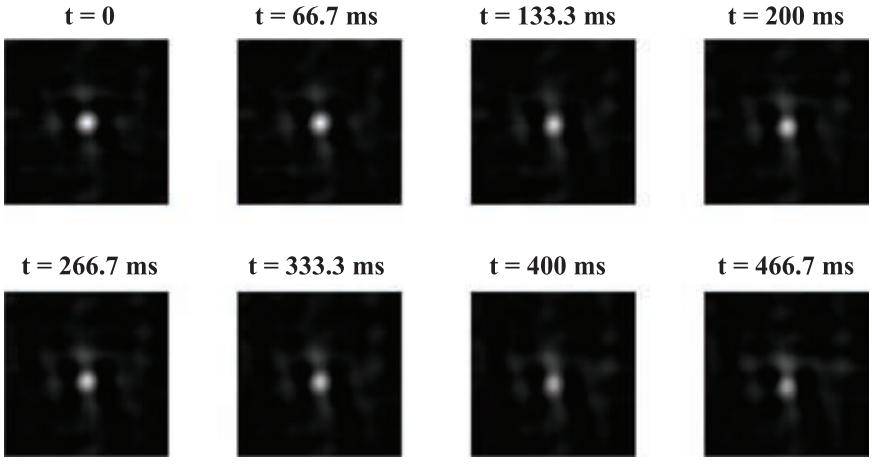

Figure 19: The change of shape in the two dimensional cross correlation function with time for the case of MVS = 37. For the evaluation, the first wavefront was taken as reference for all the calculations here.

The coordinate location of the peak (in 'x' axis) is evaluated using the following expression,

$$p = \frac{R - L}{2M - R - L} \tag{19}$$

where, $f_p(-1) = L, f_p(0) = M$ and $f_p(1) = R$ and

$$a = \frac{L + R - 2M}{2} \tag{20}$$

$$b = M - \frac{1}{8}\left[\frac{(L-R)^2}{L + R - 2M}\right] \tag{21}$$

In the case of a three point interpolator, the performance of Gaussian and parabolic interpolators is very close, unless the cross-correlation function is spread over less than 3 × 3 pixels. When a larger number of pixels around the neighbourhood of the cross correlation peak are used for interpolation, the choice of the interpolator will be critical. Another advantage of the parabolic interpolator is its ease of computation.

4.6.4 Center of gravity: For the cross-correlation matrix, $C(x, y)$, the location of the centroid (x_c, y_c) using the center of gravity (CoG) method is given by,

$$(x_c, y_c) = \frac{\sum_{ij} C_{ij} X_{ij}}{\sum_{ij} C_{ij}} \tag{22}$$

This simple peak detection technique works best with high signal to noise ratio on the cross-correlation matrix.

4.6.5 Weighted center of gravity: The weighted center of gravity (WCoG) is a method that can take the advantage of the shape information of the cross-correlation function, is an improved version of the CoG technique.

$$(x_c, y_c) = \frac{\sum_{ij} W_{ij} C_{ij} X_{ij}}{\sum_{ij} W_{ij} C_{ij}} \tag{23}$$

The technique fails for very large shifts of the peak of the cross-correlation function and under poor signal levels. Here W_{ij} is the weighting function.

4.6.6 Iteratively weighted center of gravity: This iterative technique is a more accurate extension of the WCoG technique.[43,44] This method is similar to the WCoG technique with a difference that the location of the center of the weighting function is iteratively revised in order to get closer to the actual location of the cross-correlation peak. After each iteration, the center of the weighting function is shifted to the location of the cross-correlation peak that is estimated by the previous iteration. This method of peak detection is best suited for noisy conditions and to resolve very close shifts in the peak of the cross-correlation function.

4.7 *Results*

Once the location of the peak is identified, the wind velocity can be evaluated. It can be directly derived from the slope of the straight line that best fits the curve 'x vs t' for individual MVS case as depicted in Fig. 20, for the case of parabolic interpolator. Here, the cross-correlation of wavefronts arriving at any time 't' is computed with respect to the wavefront that arrived at t = 0. It can be observed from the graph that the x-position of the cross-correlation peak increases with time for a given MVS and beyond a certain time 't', the peak detection becomes difficult due to the reduced cross-correlation maximum. For this reason, inappropriate data beyond a certain time is eliminated while fitting the 'x vs t' curve with a straight line. The slope of the 'x vs t' curve increases with increasing MVS. The maximum distance travelled along the 'x' direction by the cross-correlation peak is nearly 2 mm. The placement of the ROI at the location as indicated in Fig. 13 suggests that the shift in the peak will occur essentially due to the motion along a single direction. Similarly, the maximum shift along the 'y' direction can be calculated to be nearly 350 m. This small shift along the 'y' direction is due to the finite width of the ROI (Fig. 13).

A comparison of different peak detection techniques is shown in Fig. 21. Clearly, the overlapping Gaussian interpolator and parabolic interpolator suggest their similarity for the 3-point interpolation applied here for both cases. The CoG and WCoG methods completely fail in estimating the wind speed. This is attributed to the presence of noise in the cross-correlation matrices (see Fig. 19).

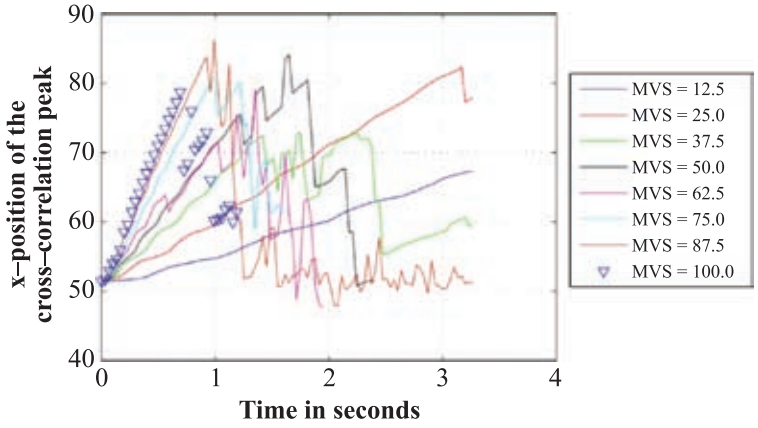

Figure 20: Parabolic interpolator: The movement of the x-coordinate of the cross correlation peak with time at different wind speed.

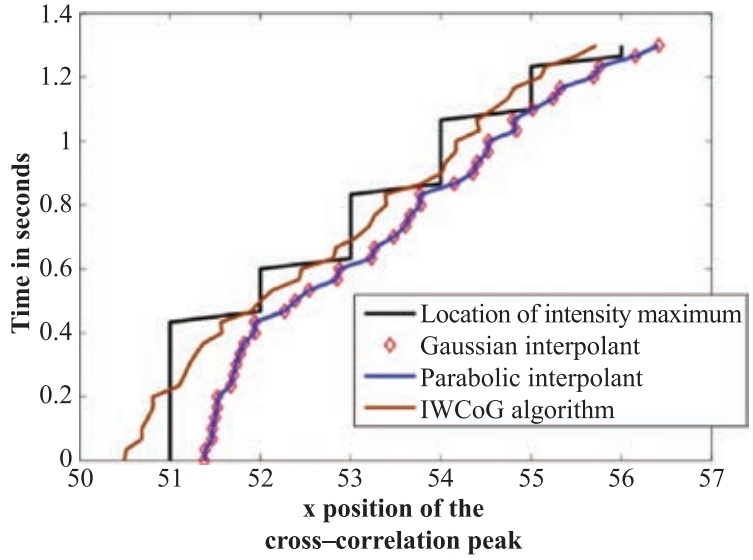

Figure 21: Comparison of peak detection techniques.

The wind speed is estimated from the measured slope values of the curve '*x* vs *t*', and are tabulated in Table 5 for parabolic interpolator and IWCoG based cross-correlation peak detection methods. The wind velocity is calculated from the slope value of the '*x* vs *t*' curve by multiplying 0.05 to it, so as to account for the bilinear interpolation performed to re-size the phase maps from 25×25 array to 100×100 matrix.

A study of the optimum time interval selection for the best estimation of wind speed for different MVS is shown in Fig. 22. This graph suggests that at very small time intervals, the measured velocity is higher than the actual (see Table 4) for all MVS, with MVS = 12.5 most affected. Hence, for lower wind speeds, the selection of a larger interval is more appropriate. This is because at lower MVS (lower wind speed), the phase plate (wavefront) moves slower and hence decaying the correlation coefficient at a slower rate. The slow decay rate of the correlation coefficient (see Fig. 17)

Table 5: Measured wind speed.

Measured wind speed	MVS actual speed (mm/s)	Parabolic method (mm/s)	IWCoG method (mm/s)
12.5	0.245	0.260	0.227
25.0	0.490	0.509	0.403
37.0	0.736	0.769	0.656
50.0	0.984	1.030	0.894
62.5	1.226	1.175	1.084
75.0	1.474	1.506	1.300
87.5	1.716	1.801	1.555
100.0	1.965	2.089	1.483

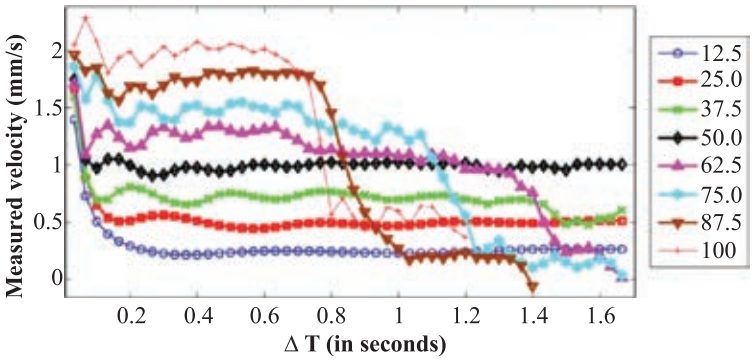

Figure 22: Parabolic interpolator: Study on the optimal choice of the time interval for wind velocity measurement at different MVS.

also indicates that the shift in the peak of the cross-correlation function is small within a small interval of time. If this shift is so small that the cross-correlation peaks cannot be resolved, the resultant measured wind speed can be erroneous. At very large time intervals and faster wind speeds, the selection of a lower time interval is better, for; there would be a risk of decorrelating the wavefronts completely if a large time interval is chosen.

At small time intervals, the IWCoG method performs better than the parabolic interpolation method. This can be concluded from the slope of the '*x* vs *t*' curve at low '*t*' for IWCoG in comparison with that for parabolic interpolation (see Fig. 21). Hence, IWCoG is sensitive to very small shifts in the peak of the cross-correlation method. Here, the Gaussian function was used as the weighting function in the IWCoG. Since the shape of the surface near the cross-correlation peak does not resemble the Gaussian for wavefronts with large time interval, IWCoG with a Gaussian weighting function is not suitable in such a case. Also, with a faster CCD, it is possible to record wavefronts at a faster rate. To take advantage of this fast nature of the detector, algorithms that detect the very small shifts in the cross-correlation peak are needed. A more rigorous analysis of the IWCoG method is necessary on the choice of weighting function, optimization of the iterations to improve the performance of the IWCoG method. As a test of repeatability, five different sets of data were analysed for each MVS listed in Table 5. It was observed that the measured wind speed was reasonably consistent with the standard deviation reducing as MVS is increased.

A plot of the measured wind speed against the actual value is shown in Fig. 23. In this plot, the data points lie along the diagonal, validating the implemented peak detection algorithms.

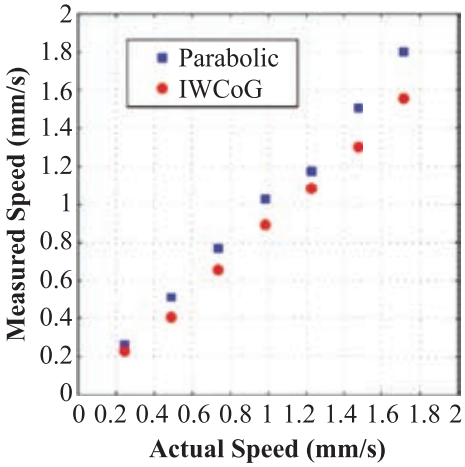

Figure 23: Validation of the parabolic interpolation and IWCoG based peak identification methods for wind velocity measurement in comparison with the actual velocity.

5 Conclusions

A technique developed for the real time measurement of wind velocity using the wavefront sensor data is described. The proposed technique was tested using numerical simulations and experimentally obtained data. The approach is based on construction of temporal correlation maps. Wind velocity is derived from vectors formed by joining the peaks of the temporally separated correlation maps within the wavefront decorrelation time. The accuracy of estimation of wind speed strongly depends on the size of the seed phase screen chosen from the initial large wavefront. It is also dependent on the number of realizations used for estimation. The use of optimum number of phase screens helps in improving the accuracy and reducing the computational time.

The peak identification technique for wind speed estimation from SHWS data was

implemented. Experimental data was obtained using the static phase plate which is mounted on a rotary stage and a laboratory SHWS. It was shown that the 3-point parabolic interpolation can be effectively used for the detection of the location of the cross-correlation peak. Optimization of the time interval that best suits with the implemented technique suggests that this method is not very sensitive to small shifts in the cross-correlation peak.

In the future, we intend to make a more detailed comparison of the peak detection technique with the other wind estimation methods, including—slope technique, frequency technique and Briggs technique which are mentioned earlier. Attempts will be made to improve the accuracy in peak detection of the cross-correlation function using better algorithms.

Received 31 January 2013.

References

1. J. W. Hardy, Adaptive optics for astronomical telescopes. Oxford University Press, USA, 1998.
2. B. L. Ellerbroek, "First-order performance evaluation of adaptive-optics systems for atmospheric-turbulence compensation in extended-field-of-view astronomical telescopes." *JOSA A* 11.2 (1994): pp. 783–805.
3. S. G. Els, et al., "Thirty Meter Telescope site testing VI: turbulence profiles." *Publications of the Astronomical Society of the Pacific* 121.879 (2009): pp. 527–543.
4. R. Racine, "Temporal fluctuations of atmospheric seeing." *Publications of the Astronomical Society of the Pacific* (1996): pp. 372–374.
5. T. Travouillon, et al., "Temporal variability of the seeing of TMT sites." *Proc. SPIE*, Ground-based and Airborne Telescopes II 7012.1 (2008): 701220.
6. J. Vernin, and C. Munoz-Tunón. "The temporal behaviour of seeing." *New Astronomy Reviews* 42.6 (1998): pp. 451–454.
7. B. García-Lorenzo, et al., "Adaptive optics parameters connection to wind speed at the Teide Observatory." *Monthly Notices of the Royal Astronomical Society* 397.3 (2009): pp. 1633–1646.
8. R. E. Hufnagel, "Variations of atmospheric turbulence." *Digest of Technical Papers*, Topical Meeting on Optical Propagation through Turbulence. 1974.
9. G. C. Valley, "Isoplanatic degradation of tilt correction and short-term imaging systems." *Applied Optics* 19.4 (1980): pp. 574–577.
10. D. P. Greenwood, "Bandwidth specification for adaptive optics systems." *JOSA* 67.3 (1977): pp. 390–393.
11. M. B. Jorgenson, and G. J. M. Aitken, "Wavefront prediction for adaptive optics." European Southern Observatory Conference and Workshop Proceedings. Vol. 48. 1994.
12. A. Vyas, M. B. Roopashree, and B. Raghavendra Prasad. "Efficient minimization of servo lag error in adaptive optics using data stream mining." *Advances in Power Electronics and Instrumentation Engineering* (2011): pp. 13–18.
13. Z. Benkhaldoun, et al., "Optical seeing monitoring at the Oukaïmeden in the Moroccan high atlas mountains: first statistics." *Astronomy and Astrophysics* 441.2 (2005): pp. 839–843.
14. Z. Benkhaldoun, "Oukaimeden as a potential observatory: Site testing results." Astronomical Site Evaluation in the Visible and Radio Range. Vol. 266. 2002.
15. B. M. Gentry, C. Huailin and X. L. Steven, "Wind measurements with 355-nm molecular Doppler lidar." *Optics letters* 25.17 (2000): pp. 1231–1233.
16. T. I. Wang, G. R. Ochs and R. S. Lawrence, "Wind measurements by the temporal cross-correlation of the optical scintillations." *Applied optics* 20.23 (1981): pp. 4073–4081.
17. S. Oya, T. Masao and A. Tadashi, "Application of an exclusively binarized correlation-calculation method to wind velocity measurement by use of stellar scintillation patterns." *Applied Optics* 40.24 (2001): pp. 4041–4049.
18. V. A. Banakh, and D. A. Marakasov, "Wind velocity profile reconstruction from intensity fluctuations of a plane wave propagating in a turbulent atmosphere." *Optics letters* 32.15 (2007): pp. 2236–2238.
19. R. V. Shack, and B. C. Platt, "Production and use of a lenticular Hartmann screen." *J. Opt. Soc. Am* 61.5 (1971): pp. 656.
20. D. Dayton, et al., "Atmospheric structure function measurements with a Shack-Hartmann wave-front sensor." *Optics letters* 17.24 (1992): pp. 1737–1739.
21. T. W. Nicholls, G. D. Boreman, and J. C. Dainty, "Use of a Shack–Hartmann wave-front sensor to measure deviations from a Kolmogorov phase spectrum." *Optics letters* 20.24 (1995): pp. 2460–2462.
22. E. E. Silbaugh, B. M. Welsh, and M. C. Roggemann, "Characterization of atmospheric turbulence phase statistics using wave-front slope measurements." *JOSA A* 13.12 (1996): pp. 2453–2460.
23. M. Schöck, and E. J. Spillar, "Measuring wind speeds and turbulence with a wave-front sensor." *Optics Letters* 23.3 (1998): pp. 150–152.
24. T. Fusco, et al., "NAOS on-line characterization of turbulence parameters and adaptive optics performance." *Journal of Optics A: Pure and Applied Optics* 6.6 (2004): pp. 585.
25. G. I. Taylor, "The spectrum of turbulence." *Proceedings of the Royal Society of London. Series A-Mathematical and Physical Sciences* 164.919 (1938): pp. 476–490.
26. E. Pinna, et al., "Simple implementation of phase screens for repeatable seeing generation." Astronomical Telescopes and Instrumentation. International Society for Optics and Photonics, 2004.
27. E. M. Johansson, and D. T. Gavel. "Simulation of stellar speckle imaging." 1994 Symposium on Astronomical

Telescopes & Instrumentation for the 21st Century. International Society for Optics and Photonics, 1994.
28. G. Sedmak, "Performance analysis of and compensation for aspect-ratio effects of fast-fourier-transform-based simulations of large atmospheric wave fronts." *Applied optics* 37.21 (1998): pp. 4605–4613.
29. G. Sedmak, "Implementation of fast-Fourier-transform-based simulations of extra-large atmospheric phase and scintillation screens." *Applied optics* 43.23 (2004): pp. 4527–4538.
30. M. C. Roggemann, and B. M. Welsh. Imaging through turbulence. CRC, 1996.
31. R. J. Noll, "Zernike polynomials and atmospheric turbulence." *J. Opt. Soc. Am* 66.3 (1976): pp. 207–211.
32. J. D. Schmidt, M. E. Goda, and B. D. Duncan. "Aberration production using a high-resolution liquid-crystal spatial light modulator." *Applied optics* 46.13 (2007): 2423–2433.
33. L. Hu, "A liquid crystal atmospheric turbulence simulator." *Optics Express* 14.25 (2006): pp. 11911–11918.
34. R. G. Lane, A. Glindemann, and J. C. Dainty. "Simulation of a Kolmogorov phase screen." Waves in random media 2.3 (1992): pp. 209–224.
35. H. L. Wu, et al., "Statistical interpolation method of turbulent phase screen." *Optics Express* 17.17 (2009): pp. 14649–14664.
36. M. B. Roopashree, A. Vyas, and B. Raghavendra Prasad. "Multilayered temporally evolving phase screens based on statistical interpolation." *Proc. SPIE*. Vol. 7736. 2010.
37. M. B. Roopashree, A. Vyas, and B. Raghavendra Prasad, "Automated ROI selection and calibration of a microlens array using a MEMS CDM." Adaptive Optics: Methods, Analysis and Applications. Optical Society of America, 2011.
38. M. B. Roopashree, A. Vyas, and B. Raghavendra Prasad, "Experimental evaluation of centroiding algorithms at different light intensity and noise levels." American Institute of Physics Conference Series. Vol. 1391. 2011.
39. W. H. Southwell, "Wave-front estimation from wave-front slope measurements." *JOSA* 70.8 (1980): pp. 998–1006.
40. R. S. Lawrence, G. R. Ochs, and S. F. Clifford, "Use of scintillations to measure average wind across a light beam". Appl. Opt. 11(2)(1972): pp. 239–243.
41. T. I. Wang, G. R. Ochs, and R. S. Lawrence. "Wind measurements bythe temporal cross-correlation of the optical scintillations". Appl. Opt. 20(23)(1981): pp. 4073–4081.
42. B. H. Briggs, G. J. Phillips and D. H. Shinn. "The analysis of observations on spaced receivers of the fading of radio signals". Proceedings of the Physical Society. Section B 63(2)(1950): pp. 106.
43. K. L. Baker, and M. M. Moallem, "Iteratively weighted centroiding for Shack-Hartmann wave-front sensors." *Optics express* 15.8 (2007): pp. 5147–5159.
44. A. Vyas, M. B. Roopashree, and B. Raghavendra Prasad, "Improved iteratively weighted centroiding for accurate spot detection in laser guide star based Shack Hartmann sensor." Atmospheric and Oceanic Propagation of Electromagnetic Waves IV 7588.1 (2010): pp. 758806.

M. B. Roopashree is a Senior Research Fellow at the Indian Institute of Astrophysics. She earned her Master's degree in 2004 from University of Mysore. She joined the Indian Institute of Astrophysics, Bangalore, as a research trainee in 2006 and later on joined the same institute as a Junior Research Fellow in 2007.

Akondi Vyas, PhD, is a Post Doctoral Research Fellow at University College Dublin since March 2012. On completion of his Bachelor's degree in 2004 at Sri Sathya Sai Institute of Higher Learning, he continued to do his Master's degree in Physics there. He was selected as a Ph.D. student under the Joint Astronomy Program at the Department of Physics, Indian Institute of Science in 2006. He moved to the Indian Institute of Astrophysics in 2007 to pursue his PhD work. During his Ph.D., he was focussed on developing advanced wavefront sensing methods for astronomical adaptive optics. Currently, he is working with Dr. Brian Vohnsen, Advanced Optical Imaging Group, University College Dublin.

B. Raghavendra Prasad, Ph.D, is Professor at Indian Institute of Astrophysics, Bangalore. He completed his B.Sc and M.Sc at Sri Sathya Sai Institute of Higher Learning and Ph.D from Indian Institute of Science. His area of research include optics, adaptive optics and astronomy instrumentation. Currently, he heads the instrumentation Division and also is the Project Manager of Visible Emission-line Space Coronagraph on Aditya-I mission.